2026 IEEE International Conference on Robotics and Automation (ICRA 2026)
June 1-5, 2026. Vienna, Austria

Proprioceptive Contact State and Contact Point Estimation for a Leg-Wheel Transformable Robot

Kuan-Jung Huang, Wei-Shun Yu, and Pei-Chun Lin*, *Senior Member, IEEE*

***Abstract*—Hybrid leg-wheel robots offer exceptional mobility, but their complex mechanics and extended contact surfaces challenge modern control frameworks that rely on simple point-foot models. Accurately estimating both the contact state and the precise contact location using only proprioceptive sensors is a critical and unresolved problem for these platforms. To address this, we present the complete, proprioception-only framework that provides both contact state and contact point information for this class of robot. The framework is executed on a computationally efficient and simplified dynamic model of the complex 11-bar leg mechanism as an example, which enables a discrete-time Generalized Momentum Observer (GMO) to accurately estimate external wrenches. An optimization-based algorithm then precisely localizes the contact point by finding the location along the rim that best explains the full-body dynamics. The framework's performance was validated in high-fidelity simulations across diverse gaits. For contact state validation, the detector demonstrates over 97% single-leg accuracy during a dynamic 0.4 m/s trot. For contact point validation, the localization stage confirms the accurate estimation throughout the stance phase with RMS 0.0173 m. Our work provides the essential contact information required to provide advanced model-based control for these challenging platforms.**

***Index Terms*—Contact Estimation, Leg-Wheel Transformable Robot, Quadruped, Robot**

I. INTRODUCTION

For legged robots, precise knowledge of the contact state—whether a foot is on the ground and where it is touching—is fundamental for achieving robust and dynamic locomotion [1], [2]. To combine the energy efficiency of wheeled systems with the adaptability of legged platforms, hybrid leg-wheel robots have emerged [3]–[6]. The leg-wheel transformable robot at the center of this study, shown in Fig.1. This platform, however, unique estimation challenges due to its mechanical complexity. First, its complex 11-bar linkage mechanism provides exceptional mobility but clashes with the simplified point-foot models required by modern controllers like Model Predictive Control (MPC) and Whole-Body Control (WBC) [7], [8]. Second, unlike classical quadrupeds [9], [10], its legs interact with the ground along a continuous wheel rim, invalidating the common point-foot assumption.This creates a critical ambiguity: since the relationship between actuator torques (τ) and ground reaction forces (GRF, F_{ext}) is mediated by the Jacobian transpose at the unknown contact location ($J(q)^T$), the controller cannot accurately solve the inverse dynamics problem for force control.This creates a critical gap: to effectively control this robot, an estimation framework is needed to translate its complicated physical interactions into the simplified abstractions that controllers can understand.

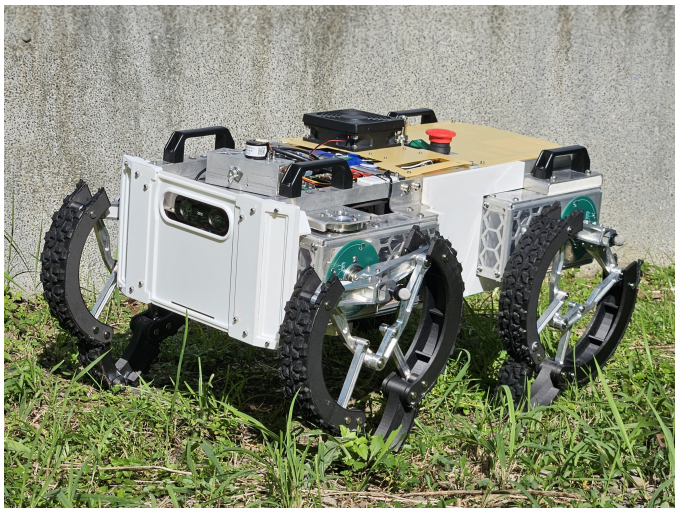

Fig. 1: The leg-wheel transformable robot investigated in this work.

In recent years, proprioceptive sensing has become a dominant approach for contact estimation, avoiding the fragility and cost of external sensors [11]–[13] For collision detection, a common strategy involves using a dynamics-based observer, such as the Generalized Momentum Observer (GMO) [14]–[16]. And for leg contact estimation often processed GRF by a probabilistic framework, such as Hidden Markov Model [17], [18] or simply use the learning-based classifier [19]—to produce a binary classification of the contact state (i.e., swing or stance).However, the majority of this research answers the question "is the leg in contact?" but does not provide the crucial spatial information required for robots with extended contact surfaces. While methods like the Contact Particle Filter (CPF) [20], have addressed proprioceptive contact point localization using a stochastic search, the specific kinematics of our leg-wheel system—where contact is constrained to a rim with a discontinuous Jacobian—make such a global search computationally prohibitive.

To address this gap, this paper presents a complete, proprioception-only framework for high-accuracy contact state detection and precise contact point localization, particularly

This work was supported by the National Science and Technology Council (NSTC), Taiwan, under Contracts 112-2221-E-002-136-MY3.

The authors are with the Department of Mechanical Engineering, National Taiwan University, Taipei 10617, Taiwan (*corresponding author email: peichunlin@ntu.edu.tw).

TABLE I: The robot specifications

Parameter		Value	Unit
Weight	Body	19.00	kg
	Leg-Wheel (each)	0.68	
Body Dimension	Length	0.62	m
	Width	0.33	
	Height	0.17	
Wheelbase	X-direction	0.444	m
	Y-direction	0.386	
Leg-Wheel	Radius	0.12	m
	Max Extension	0.34	

suited for robotic systems with extended or geometrically complex contact surfaces. We demonstrate the efficacy and practicality of this framework by applying it to a challenging case study: a leg-wheel transformable robot featuring a complex 11-bar linkage and continuous rim contact. The main contributions of this work are:

- **An enabling simplified dynamic model:**We introduce a computationally efficient dynamic model that, for our challenging case study, successfully abstracts a complex 11-bar leg-wheel mechanism into a form compatible with standard model-based estimators, making the use of a GMO for accurate wrench estimation feasible during dynamic motion.
- **A deterministic contact point localization algorithm:** In contrast to stochastic approaches, we propose a general, optimization-based algorithm that leverages parameterized contact geometry to deterministically find the location that best explains the wrench observed from the robot's full-body dynamics.
- **The design and validation of a complete estimation pipeline:**We demonstrate the efficacy of our full three-stage pipeline (wrench estimation $\rightarrow$ state detection $\rightarrow$ point localization) through high-fidelity simulation of our case study, showing robust and accurate performance across various dynamic gaits.

The remainder of this paper is organized as follows. Section II details the robot's kinematic and dynamic models. Section III presents our proposed three-stage contact estimation framework. Section IV describes the simulation experiments and discusses the results, and Section V concludes the paper with directions for future work.

II. Modeling and Problem Formulation

A. The Brief Review of The Robot

The platform investigated in this work is a leg-wheel transformable quadruped robot, shown in Fig. 1. The robot architecture consists of a central body and four identical leg-wheel modules. Each module is actuated by two DC brushless motors, enabling complex locomotion capabilities. The key physical parameters and specifications of the robot are summarized in Table I. The kinematic configuration of the leg-wheel module is illustrated in Fig. 2. The mechanism is a planar 11-bar linkage with 2-DOF (degree of freedom), actuated by two motors co-located at the leg's origin, point O. The motors

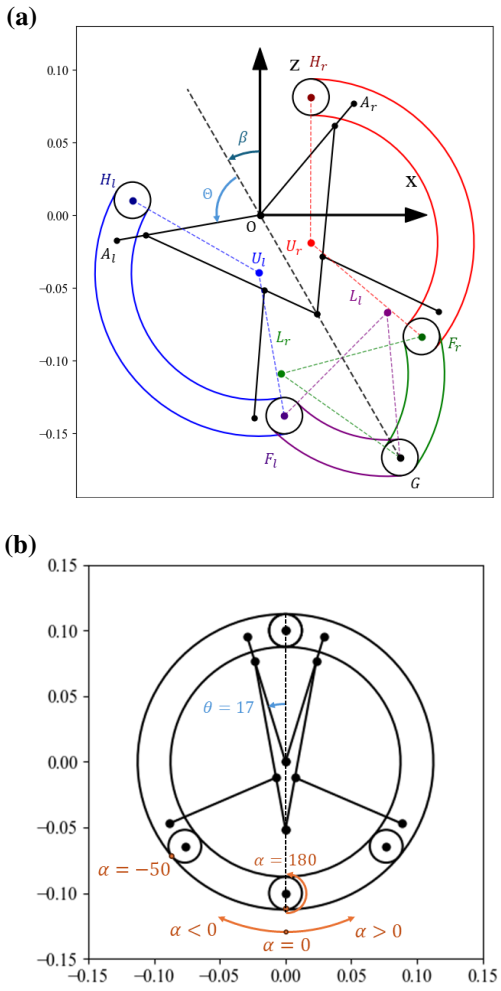

Fig. 2: The Kinematic model and contact geometry of the leg-wheel: (a) illustrating the generalized coordinates (θ, β) and identifies the five potential contact surfaces: upper left rim (blue) , upper right rim (red) , lower left rim (purple), lower right rim (green) , and the toe point (G). (b) defining the local coordinate α used to specify a unique point along these rims.

directly drive the links OA_R and OA_L, and their respective angular positions define the actuation vector $\mathbf{\Phi} = [\phi_R, \phi_L]^T$. For a more intuitive parameterization of the leg's state, we introduce a generalized coordinate system $\boldsymbol{\eta} = [\theta, \beta]^T$. As shown in Fig. 2, β represents the overall rotation of the leg's primary axis relative to the vertical, while θ describes the symmetric expansion or retraction of the leg, when $\theta = \theta_0 = 17°$, the leg in wheel mode.The physical limits of the mechanism constrain the expansion angle to $\theta \in [17°, 160°]$. This transformation from the motor coordinates to the generalized coordinates is defined by the linear relationship in (1):

$$\boldsymbol{\eta} = \begin{bmatrix} \theta \\ \beta \end{bmatrix} = \frac{1}{2} \begin{bmatrix} 1 & -1 \\ 1 & 1 \end{bmatrix} \begin{bmatrix} \phi_R \\ \phi_L \end{bmatrix} + \begin{bmatrix} 1 \\ 0 \end{bmatrix} \theta_0 \tag{1}$$

Unlike conventional quadrupeds, the robot has an extended contact surface. As depicted in Fig. 2(a), the leg-wheel can contact the ground in five ways: via the upper left rim (blue), upper right rim (red), lower left rim (purple), lower right rim (green), or the toe point (**G**).

Consider real-time computation of the leg's kinematics, the Cartesian positions of the centers of these key rims (H_l, H_r, F_l, F_r, G) are pre-calculated and fitted as functions of the generalized coordinate θ. This approach provides a computationally efficient method for determining the geometric state of the leg.

Furthermore, to uniquely identify any potential contact point on these surfaces, we parameterize the rims using an angle $\alpha \in [-\pi, \pi]$, as illustrated in Fig. 2(b). For the main rims, the local coordinate α is defined such that $\alpha = 0$ corresponds to the intersection of the rim and the ray originating from the lower-left joint (L_l) passing through the toe point (G). As the leg mechanism extends, the physical configuration of the linkage exposes an additional curved contact surface. To properly model this interaction, we define a local $\alpha \in [0, \pi]$ for the area surrounding point G, ensuring the framework can localize contact points even as the leg's effective contact geometry changes during expansion.

B. The Simplified Model

To enable real-time estimation and control, the robot is simplified from a 14-DOF to a 12-DOF system by ignoring the lateral translation (y) and yaw rotation, as the robot is primarily designed for planar locomotion while in leg mode. This modeling approach for a single leg was first proposed and validated against a real-world module in [21]. The present work extends this reduced-order leg model to a full-body dynamic model, which consists of a 4-DOF floating base and four simplified legs, as illustrated in Fig. 3 (c).

1) Leg Model: Each leg is abstracted as a RP model. The leg's configuration is described by two generalized coordinates: the rotation of the leg's primary axis, β, and its prismatic extension. This extension is represented by the distance from the hip joint (O) to the leg's center of mass (COM), denoted as R_m. Both R_m and the leg's moment of inertia about its COM, I_c, are functions of the generalized expansion coordinate θ (defined in Section II-A). To capture their behavior, these relationships were modeled by fitting the data from the full rigid body model to fourth-order polynomials:

$$R_m(\theta) = A_4\theta^4 + A_3\theta^3 + A_2\theta^2 + A_1\theta + A_0 \tag{2}$$

$$I_c(\theta) = B_4\theta^4 + B_3\theta^3 + B_2\theta^2 + B_1\theta + B_0 \tag{3}$$

The result of fitted relationships shows in Fig. 3 (a)(b). The kinematics of this simplified leg relate the operational space coordinates $\boldsymbol{q}_{leg} = [\beta, R_m]^T$ to the generalized coordinates $\boldsymbol{\eta} = [\theta, \beta]^T$. The velocity and acceleration relationships are given by:

$$\dot{\boldsymbol{q}} = \begin{bmatrix} 0 & 1 \\ 4A_4\theta^3 + 3A_3\theta^2 + 2A_2\theta + A_1 & 0 \end{bmatrix} \begin{bmatrix} \dot{\theta} \\ \dot{\beta} \end{bmatrix} \tag{4}$$

$$\begin{aligned} \ddot{\boldsymbol{q}} = &\begin{bmatrix} 0 & 1 \\ 12A_4\theta^2 + 6A_3\theta + 2A_2 & 0 \end{bmatrix} \begin{bmatrix} \dot{\theta}^2 \\ \dot{\beta}^2 \end{bmatrix} \\ &+ \begin{bmatrix} 0 & 1 \\ 4A_4\theta^3 + 3A_3\theta^2 + 2A_2\theta + A_1 & 0 \end{bmatrix} \begin{bmatrix} \ddot{\theta} \\ \ddot{\beta} \end{bmatrix} \end{aligned} \tag{5}$$

The relationship between the actuator torques and the generalized forces in the leg's operational space, $[\tau_\beta, F_{R_m}]^T$, is derived using the principle of virtual work, which relates forces and torques through the transpose of the kinematic Jacobians J_Φ, J_η:

$$\begin{aligned} \dot{\eta} &= J_\Phi \dot{\Phi} \\ \dot{q_{leg}} &= J_\eta \dot{\eta} \end{aligned} \tag{6}$$

$$\begin{bmatrix} \tau_\beta \\ F_{R_m} \end{bmatrix} = (J_\eta{}^T)^{-1} (J_\Phi{}^T)^{-1} \begin{bmatrix} \tau_{\phi_R} \\ \tau_{\phi_L} \end{bmatrix} \tag{7}$$

2) Floating Base Model: To develop a more focused and computationally efficient model, we first analyzed the robot's principal dynamics. The robot is primarily designed for motion within the plane, and its leg modules are engineered to generate forces exclusively along the X (forward) and Z (vertical) axes. Since both the intended movement and the actuation capabilities are constrained to X-Z plane, the most significant dynamics are the planar translations along X and Z, and the associated rotations of roll (ϕ) and pitch (ψ). Based on this analysis, the robot's floating base can be simplified to a 4-DOF rigid body that captures these essential degrees of freedom.

3) Full System State: Combining these components, the full robot model has a total of 12 degrees of freedom. The generalized coordinate vector $\boldsymbol{q} \in \mathbb{R}^{12}$ is defined as the concatenation of the base state, $\boldsymbol{q}_{base} = [x, z, \phi, \psi]^T$, and the four individual leg states, $\boldsymbol{q}_{leg,i} = [\beta_i, R_{m,i}]^T$:

$$\boldsymbol{q} = [\boldsymbol{q}_{base}^T, \boldsymbol{q}_{leg,i}^T]^T \tag{8}$$

where $i \in \{LF, RF, LH, RH\}$ denotes Left-Front (LF), Right-Hind (RH), Right-Front (RF) and Left-Hind (LH) leg respectively.

4) Simplified Full-Body Dynamics: The equations of motion for the 12-DOF simplified model are derived using the Euler-Lagrange formulation:

$$\begin{aligned} \boldsymbol{M}(\boldsymbol{q})\ddot{\boldsymbol{q}} + \boldsymbol{C}(\boldsymbol{q}, \dot{\boldsymbol{q}})\dot{\boldsymbol{q}} + \boldsymbol{D}(\dot{\boldsymbol{q}}) + \boldsymbol{g}(\boldsymbol{q}) \\ = \boldsymbol{S}^{\boldsymbol{T}}\boldsymbol{\tau} + \sum_i \boldsymbol{J}_{\boldsymbol{i}}^T(\boldsymbol{q})\boldsymbol{F}_i^{ext} \end{aligned} \tag{9}$$

- $\boldsymbol{M}(\boldsymbol{q}) \in \mathbb{R}^{12\times12}$ is the mass matrix.
- $\boldsymbol{C}(\boldsymbol{q}, \dot{\boldsymbol{q}})\dot{\boldsymbol{q}} \in \mathbb{R}^{12\times12}$ represents the Coriolis and centrifugal forces. Computed using Christoffel symbols and formed by proper factorization such that $\dot{M} - 2C$ is skew-symmetric.
- $\boldsymbol{g}(\boldsymbol{q}) \in \mathbb{R}^{12}$ is the vector of gravitational forces.
- $\boldsymbol{S}^{\boldsymbol{T}}\boldsymbol{\tau}$ is the vector of actuator input, where $\boldsymbol{\tau} \in \mathbb{R}^8$ are motor torques, and $\boldsymbol{S} \in \mathbb{R}^{8\times12}$ is the selection matrix.
- $\boldsymbol{J}_{\boldsymbol{i}}^T(\boldsymbol{q})\boldsymbol{F}_i^{ext}$ represents the effect of external contact forces, where i denotes the index of the specific contact point.

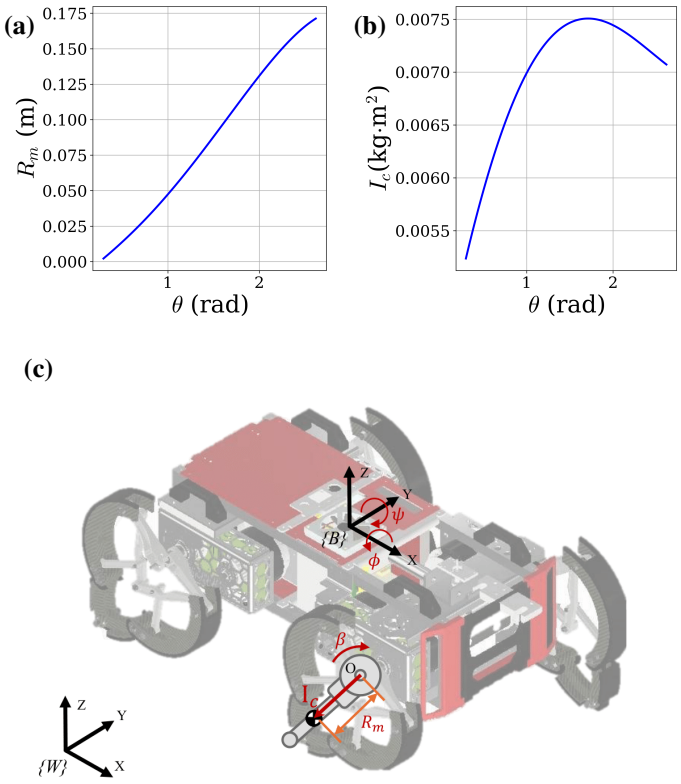

Fig. 3: (a) Fitted relationships between the leg's COM distance R_m and expansion angle θ. (b) Fitted relationships between COM inertia I_c and expansion angle θ. (c) The simplified full-body model, illustrating the 4-DOF floating base with its coordinate frame $\{B\}$ and the reduced-order RP model for RF leg.$\{W\}$ denotes the world coordinate frame.

The leg's moment of inertia, $I_c(\theta)$, is modeled using polynomial fit. Its time derivative, $\dot{I}_c$, therefore introduces velocity-dependent terms not typically found in standard rigid-body models, which are included into $\boldsymbol{D}(\dot{\boldsymbol{q}})$. However, these terms are considered negligible because their magnitude is small in comparison to other dynamic terms.

III. The Contact Estimation Framework

Our proposed framework for contact estimation is a three-stage process. First, a discrete-time GMO estimates the generalized external forces acting on each leg. Second, the magnitude of these estimated forces is used to detect the contact state of each leg. Finally, for legs determined to be in contact, an optimization-based method is employed to localize the precise contact point along the leg's rim. The details of each stage are presented below.

A. The External Force Estimation

To estimate external forces during highly dynamic gaits, we employ the discrete-time Generalized Momentum-based (GM-based) Disturbance Observer proposed by Bledt et al. [11]. This approach directly reformulates the observer in the discrete domain, avoiding significant errors that arise from the simple discretization of its continuous-time counterpart, particularly during rapid leg swings. By leveraging summation by parts, this method bypasses the need for noisy acceleration measurements, leading to more accurate and robust force estimates.

The observer aims to estimate the generalized disturbance, $\boldsymbol{\tau}_d$, which is assumed to be the result of all external contact forces, $\boldsymbol{F}_{ext}$:

$$\boldsymbol{\tau}_d = \sum_i \boldsymbol{J}_i^T(\boldsymbol{q})\boldsymbol{F}_i^{ext} \tag{10}$$

The final discrete-time observer provides an estimate of this disturbance at each time step k using the following expression:

$$\hat{\boldsymbol{\tau}}_{d,k} = \beta \boldsymbol{p}_k - \frac{(1-\gamma)}{1-\gamma z^{-1}}(\beta \boldsymbol{p} + S^T\boldsymbol{\tau} - C^T\dot{\boldsymbol{q}} - G) \tag{11}$$

where $\hat{\boldsymbol{\tau}}_{d,k}$ is the estimated disturbance torque, and $\boldsymbol{p}_k = M(\boldsymbol{q}_k)\dot{\boldsymbol{q}}_k$ is the generalized momentum. The term z^{-1} represents the unit delay operator. The observer gains, $\beta = \frac{(1-\gamma)\gamma^{-1}}{\Delta t}$ and $\gamma = e^{-\lambda \Delta t}$, are determined by the desired cutoff frequency λ and the system's sampling time Δt.

We validated our simplified model and the observer in simulation, in which we use a highly dynamic trotting gait with 0.4 m/s speed. Figure 4 shows the results during a dynamic swing phase, where the true external contact force is expected to be zero. The "Raw F_{R_m}" represents a naive disturbance calculation. To clarify, F_{R_m} denotes the generalized force in the prismatic joint of the simplified RP-model. During a rapid swing, the motors must exert significant torques to accelerate and decelerate the leg's linkages. Without an observer that properly accounts for the system's own dynamics (i.e., inertial and Coriolis effects), these large internal actuation forces are incorrectly interpreted as external contact forces, resulting in the erroneous spikes seen in the plot.

In contrast, the "Estimated Disturbance F_{R_m}" is the final output from our observer. By leveraging the dynamic model, the observer correctly subtracts the forces required for the leg's own movement. The remaining signal, which represents the true external force, stays close to zero as expected. This result confirms that our simplified model and observer work accurately distinguish between internal dynamic forces and genuine external contacts.

B. The Leg Contact State Detection

Once the generalized external wrench, $\hat{\boldsymbol{\tau}}_{d,k}$, is estimated by the GM-based Disturbance Observe, the next stage is to determine the contact state (Stance or Swing) for each leg. The estimated wrench vector is first decomposed to isolate the components corresponding to each leg $i \in \{LF, RF, LH, RH\}$, yielding an individual leg wrench, $\hat{\boldsymbol{\tau}}_{leg,i} = [\hat{\tau}_{\beta,i}, \hat{F}_{R_m,i}]^T$.

A threshold-based classifier is then applied to these components. A leg is determined to be in contact with the ground if either the estimated rotational torque, $\hat{\tau}_{\beta,i}$, or the prismatic force, $\hat{F}_{R_m,i}$, exceeds its respective predefined threshold. This logical condition can be expressed as:

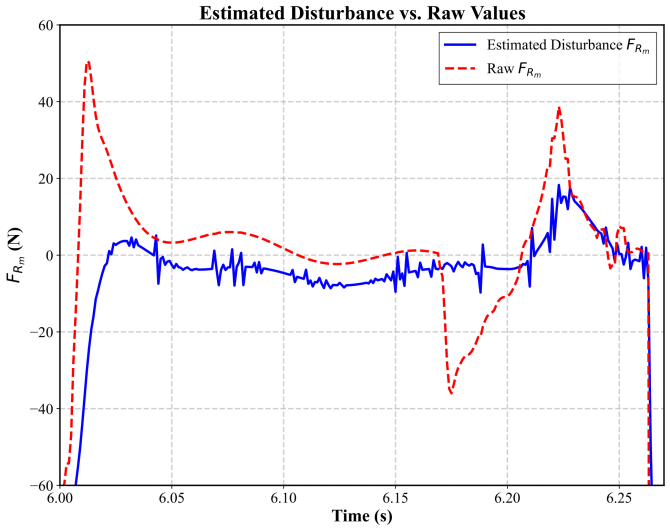

Fig. 4: Validation of the discrete-time GMO of the simplified model during the single-leg swing phase of the Left-Front (LF) leg.

$$\text{Contact State}_i = \begin{cases} \text{Stance}, & \text{if } (|\hat{\tau}_{\beta,i}| > \varepsilon_\tau) \vee (|\hat{F}_{R_m,i}| > \varepsilon_F) \\ \text{Swing}, & \text{otherwise} \end{cases} \tag{12}$$

where ε_τ and ε_F are the thresholds for the rotational torque and prismatic force, respectively. The thresholds ε_τ and ε_F were determined empirically by analyzing the peak disturbance signals during the swing phase in simulation. The use of absolute values ensures that both positive and negative forces, corresponding to different contact scenarios, are detected.

The selection of these thresholds is critical for robust performance. Because the leg's geometry is abstracted into a rotational joint (β) and a prismatic joint (R_m), the location of a contact on the rim has a different effect on the two components of the estimated wrench, $\hat{\tau}_{leg,i} = [\hat{\tau}_{\beta,i}, \hat{F}_{R_m,i}]^T$.The set of legs identified as being in the Stance state is then passed to the contact point localization algorithm.

C. The Contact Point Localization

Once a leg has been identified as being in the stance phase, this final stage aims to localize the precise contact point along its rim, which we parameterize by the angle α. The core of our method is to find the set of contact points (one for each contacting leg) that best explains the total external wrench observed on the robot's body.

1) The Mapping to Actuator and Candidate Contact Forces: For each contacting leg $i \in \mathscr{C}$, we begin with the estimated external wrench in the simplified RP-space, $\hat{\tau}_{leg,i} = [\hat{\tau}_{\beta,i}, \hat{F}_{R_m,i}]^T$. Using the principle of virtual work, we first map this wrench to the equivalent external torques, $\hat{\tau}_{\Phi,i} = [\hat{\tau}_{\phi_R,i}, \hat{\tau}_{\phi_L,i}]^T$, that would be experienced at the two drive motors:

$$\hat{\tau}_{\Phi,i} = (J_\Phi^T)^{-1}(J_\eta^T)^{-1}\hat{\tau}_{leg,i} \tag{13}$$

With these estimated external motor torques, we can generate a field of candidate contact forces across the leg's rim, as visualized in Fig. 5. For any potential contact point $P(\alpha)$ on the rim, the corresponding Cartesian force $\boldsymbol{F}_p(\alpha) = [F_x, F_z]^T$ that would produce these motor torques can also be found via virtual work [22]:

$$\boldsymbol{F}_p(\alpha) = (J_p(\alpha)^T)^{-1}\hat{\tau}_{\Phi,i} \tag{14}$$

where $J_p(\alpha) = \partial P(\alpha)/\partial \boldsymbol{\Phi}$ is the Jacobian mapping motor velocities to the Cartesian velocity of the point $P(\alpha)$.

2) The Fast Kinematic Mapping for Jacobian Calculation: To compute the Jacobian $J_p(\alpha)$ efficiently in real-time, we utilize a piecewise kinematic model based on the leg's fitted geometry. The position of any point on the rim, $\boldsymbol{P}_\theta$, is first defined in a nominal, non-rotated frame ($\beta = 0$) as a function of the expansion angle θ and the rim parameter α:

$$\boldsymbol{P}_\theta(\alpha,\theta) = \begin{cases} \text{Rot}(\alpha+\pi)\cdot \vec{U_l H_l} + \boldsymbol{U_l}, & \text{at Left Upper Rim} \\ \text{Rot}(\alpha)\cdot \vec{L_l G} + \boldsymbol{L_l}, & \text{at Left Lower Rim} \\ \text{Rot}(\alpha)\cdot \vec{L_l G} + \boldsymbol{G}, & \text{at Toe Point (G)} \\ \text{Rot}(\alpha)\cdot \vec{L_r G} + \boldsymbol{L_r}, & \text{at Right Lower Rim} \\ \text{Rot}(\alpha-\pi)\cdot \vec{U_r H_r} + \boldsymbol{U_r}, & \text{at Right Upper Rim} \end{cases} \tag{15}$$

The final position of the point in the hip frame, $\boldsymbol{P}_\eta$, is found by applying the leg's overall rotation, β:

$$\boldsymbol{P}_\eta(\alpha,\theta,\beta) = \text{Rot}(\beta)\cdot \boldsymbol{P}_\theta(\alpha,\theta) \tag{16}$$

The Jacobian $J_p(\alpha)$ is then analytically derived from these kinematic relationships.

3) Optimization Problem Formulation: The net external wrench acting on the robot's body, $\boldsymbol{W}_{body} = [F_x, F_z, \tau_\phi, \tau_\psi]^T$, can be independently estimated from the full-body dynamics and IMU data. We assume this net wrench is the sum of the wrenches produced by a single contact force on each leg in the set $\mathscr{C}$.

For each 2D candidate contact force $\boldsymbol{F}_{p,i}(\alpha_i) = [F_x, F_z]^T$ on leg i, its contribution to the 4-DOF body wrench, $\boldsymbol{W}_i \in \mathbb{R}^4$, is calculated. This transformation is defined by the contact point's position vector relative to the body's center of mass, $\boldsymbol{P}_{body,i}(\alpha_i) = [x_i, y_i, z_i]^T$. The mapping is given by the transpose of the body Jacobian:

$$\boldsymbol{W}_i(\alpha_i) = \begin{bmatrix} 1 & 0 \\ 0 & 1 \\ 0 & y_i \\ z_i & -x_i \end{bmatrix} \begin{bmatrix} F_x \\ F_z \end{bmatrix} = \begin{bmatrix} F_x \\ F_z \\ y_i F_z \\ z_i F_x - x_i F_z \end{bmatrix} \tag{17}$$

The resulting wrench vector $\boldsymbol{W}_i = [F_x, F_z, \tau_\phi, \tau_\psi]^T$ directly corresponds to the generalized forces acting on the simplified 4-DOF body model.

The optimal set of contact points $\{\alpha_i^*\}_{i\in\mathscr{C}}$ is found by minimizing a residual vector, $\boldsymbol{\gamma}$, which represents the difference between the wrench observed from the IMU and full-body dynamics, $\boldsymbol{W}_{body}$, and the wrench reconstructed from a set of candidate contact points, $\{\alpha_i\}$.

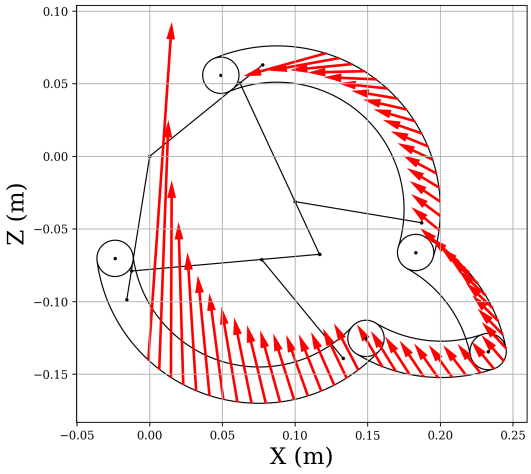

Fig. 5: The candidate contact force (i.e., red arrows) on a single leg.

TABLE II: Contact State Detection Accuracy

Gait	Single Leg Avg. Acc.	Overall Acc.
Walk (0.1 m/s)	99.16%	96.76%
Hybrid Gait (0.12 m/s)	95.04%	80.28%
Trot (0.4 m/s)	97.30%	89.20%
Climb	92.60%	79.24%

A simple squared norm minimization of this residual treats all components (linear forces and rotational torques) equally. However, the roll and pitch torques, while critical for balance, are often numerically smaller than the force components and could be underestimated in the optimization. To address this, we introduce a diagonal weighting matrix, $\mathbf{W}$, to selectively penalize errors in the rotational terms more heavily. The optimization problem is therefore formulated as finding the set of contact points that minimizes this weighted squared residual:

$$\begin{aligned} \underset{\{\alpha_i\}_{i\in\mathscr{C}}}{\text{minimize}} \quad & \gamma(\{\alpha_i\})^T \mathbf{W} \gamma(\{\alpha_i\}) \\ \text{subject to} \quad & \alpha_i \in [-\pi, \pi], \quad \forall i \in \mathscr{C} \end{aligned} \tag{18}$$

where $\mathbf{W} = \text{diag}(1, 1, w, w)$ with the weight for roll and pitch, $w > 1$. To solve this, we discretize contact points on each rim into N candidate points and perform a search over all combinations to find the set $\{\alpha_i^*\}$ that minimizes this weighted cost function.

IV. Validation of the Proposed Methodology

To validate the proposed contact estimation framework, we conducted a series of experiments in a realistic simulation environment.

A. Simulation Environment Setup

All experiments were conducted in the Webots robotics simulator, which utilizes the Open Dynamics Engine (ODE) for physics calculations. The simulated robot model was designed to closely match the physical hardware, with inertial properties such as mass and inertia tensors identified from the CAD model.

The actuators were modeled as torque-controlled DC motors

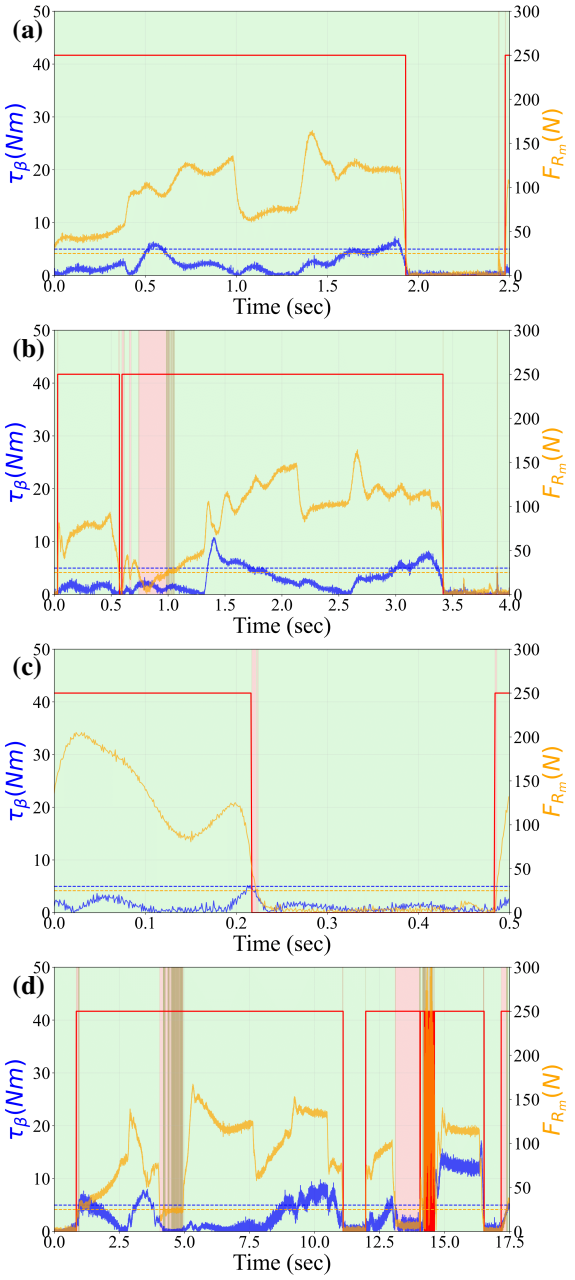

Fig. 6: The Single-leg contact state detection results for different gaits.(a) Walk gait at 0.1 m/s. (b) Hybrid gait at 0.12 m/s. (c) Trot gait at 0.4 m/s. (d) climb. Here, the leg LF was utilized as the example. For each leg, the estimated rotational disturbance (τ_β) and prismatic disturbance (F_{R_m}) are plotted as solid blue and orange lines, respectively, with their corresponding thresholds shown as dashed lines. The background color indicates the correctness of the classification (green: correct, red: incorrect) against the ground truth contact state (solid red line, high value for contact).

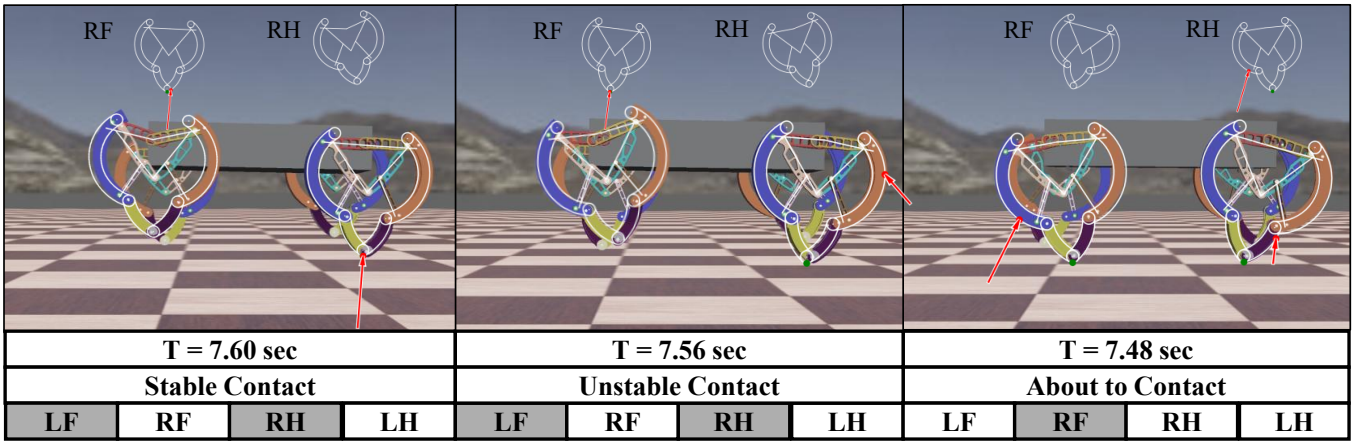

Fig. 7: Contact point localization during a dynamic trot (0.4 m/s), highlighting critical moments during gait transitions. (A supplementary video shows the complete sequence.) Green dots represent the ground truth contact points, while red dots show our estimates. Red arrows indicate the estimated contact force at each localized point. The rows at the bottom provide context: time (top), gait phase (middle), and the detected contact state for each leg (bottom: white for stance, grey for swing).

that track high-level position commands via a PID controller. This control architecture mirrors the one implemented on the physical hardware. The simulated sensors were configured to mimic real-world conditions; data from motor encoders, torque feedback, and the IMU were sampled at 1000 Hz, and zero-mean Gaussian noise was added to all sensor outputs. The specific noise standard deviations are detailed in Table III.

TABLE III: Simulated Sensor Noise Parameters

Sensor	Parameter	Value
IMU	Gyroscope Std. Dev.	0.01 rad/s
	Accelerometer Std. Dev.	0.008 m/s^2
	Attitude Std. Dev.	0.00873 rad
Motor	Encoder Std. Dev.	0.0015 rad
	Torque Feedback Std. Dev.	0.01 Nm

B. The Leg Contact State Detection

We evaluated the performance of our contact state detector across several distinct gaits: a slow walk (0.1 m/s), a dynamic trot (0.4 m/s), a hybrid gait, in which use mainly use lower rim to contact, and a challenging stair climb (3 steps, 0.12 m height each), which was developed by [23]. The same set of force and torque thresholds ($\varepsilon_F, \varepsilon_\tau$) was used for all experiments to test the robustness of the method. We report two metrics: *Single Leg Average Accuracy*, which is the average classification accuracy over the four individual legs, and *Overall Contact State Accuracy*, which measures the percentage of time steps where the contact states of all four legs were correctly identified simultaneously, the accuracy calculate the result of each gait in a one period, and climbing one step in stair climb challenge.

The quantitative results in Table II demonstrate our method's high accuracy, especially during walk and trot.Fig. 6 provides a qualitative view of this performance, plotting the estimated disturbances, F_{R_m} and τ_β, against their thresholds for the Left-Front (LF) leg.

This visualization confirms that, for both walking and trotting, most detection errors are confined to the brief phase transitions at touchdown and lift-off. During these moments, the contact is inherently unstable and ground reaction forces are minimal, making a precise classification challenging. Despite this, the detector correctly identifies the state for the vast majority of the gait cycle.

The stair climb primary challenge arises when the robot utilizes its upper rim for contact. Due to the leg's complex kinematics, forces on this part of the rim produce a less pronounced signature in the motor torques, making detection inherently more difficult. Nevertheless, the results validate the detector's effectiveness across a wide range of both common and highly specialized contact situations.

C. Contact Point Localization

The performance of the contact point localization algorithm was evaluated during a dynamic trot at 0.4 m/s. For the optimization search, we sampled 55 candidate points on the rim of each contacting leg. These points were distributed by starting at the center of the main lower rim (point G) and sampling outwards every five degrees. As shown in Fig. 7, the algorithm accurately estimates the contact location during stable stance phases, with an RMS localization error of 0.0173 m.

The primary source of error in this stage is closely tied to the accuracy of the contact state detector. Fig. 7 illustrates a challenging moment during gait transition: as the LF and RH legs are lifting off, the RF and LH legs are touching down. An instantaneous misclassifications of a leg's contact state (e.g., believing a leg is in stance when it is in swing) can lead to an over-constrained or ill-posed optimization problem, resulting in temporary errors in the estimated contact points.

V. Conclusion and Future Work

In this paper, we presented a comprehensive, proprioception-only framework to resolve both contact state and contact point for a leg-wheel transformable robot. Our approach combines a simplified dynamic model with a discrete-time Generalized Momentum Observer for accurate wrench estimation, followed by a optimization algorithm for precise contact localization. High-fidelity simulations validated the framework's effectiveness, demonstrating over 97% single-leg contact detection accuracy during a dynamic 0.4 m/s trot and a precise 0.0173 m RMS error in contact point localization.

Future work will focus on extending the current instantaneous estimation to a time-series problem, for instance, by incorporating a filtering approach. This will improve the stability and continuity of the contact estimation. Ultimately, this more precise and reliable contact information will serve as a crucial foundation for implementing high-performance force control, significantly enhancing the robot's ability to delicately and robustly interact with its environment.

References

[1] J. Di Carlo, P. M. Wensing, B. Katz, G. Bledt, and S. Kim, "Dynamic locomotion in the mit cheetah 3 through convex model-predictive control," in *2018 IEEE/RSJ International Conference on Intelligent Robots and Systems (IROS)*. IEEE, 2018, pp. 1–9.

[2] D. Kim, J. Di Carlo, B. Katz, G. Bledt, and S. Kim, "Highly dynamic quadruped locomotion via whole-body impulse control and model predictive control," *arXiv preprint arXiv:1909.06586*, 2019.

[3] S.-C. Chen, K.-J. Huang, W.-H. Chen, S.-Y. Shen, C.-H. Li, and P.-C. Lin, "Quattroped: a leg–wheel transformable robot," *IEEE/ASME Transactions On Mechatronics*, vol. 19, no. 2, pp. 730–742, 2013.

[4] W.-H. Chen, H.-S. Lin, Y.-M. Lin, and P.-C. Lin, "Turboquad: A novel leg–wheel transformable robot with smooth and fast behavioral transitions," *IEEE Transactions on Robotics*, vol. 33, no. 5, pp. 1025–1040, 2017.

[5] R. Cao, J. Gu, C. Yu, and A. Rosendo, "Omniwheg: An omnidirectional wheel-leg transformable robot," in *2022 IEEE/RSJ International Conference on Intelligent Robots and Systems (IROS)*, 2022, pp. 5626–5631.

[6] Y. Shi, M. Zhang, M. Li, and X. Zhang, "Design and analysis of a wheel-leg hybrid robot with passive transformable wheels," *Symmetry*, vol. 15, no. 4, 2023.

[7] S. Kuindersma, R. Deits, M. Fallon, A. Valenzuela, H. Dai, F. Permenter, T. Koolen, P. Marion, and R. Tedrake, "Optimization-based locomotion planning, estimation, and control design for the atlas humanoid robot," *Autonomous robots*, vol. 40, no. 3, pp. 429–455, 2016.

[8] M. Focchi, A. Del Prete, I. Havoutis, R. Featherstone, D. G. Caldwell, and C. Semini, "High-slope terrain locomotion for torque-controlled quadruped robots," *Autonomous Robots*, vol. 41, no. 1, pp. 259–272, 2017.

[9] B. Reagen, W.-S. Choi, Y. Ko, V. T. Lee, H.-H. S. Lee, G.-Y. Wei, and D. Brooks, "Cheetah: Optimizing and accelerating homomorphic encryption for private inference," in *2021 IEEE International Symposium on High-Performance Computer Architecture (HPCA)*, 2021, pp. 26–39.

[10] M. Hutter, C. Gehring, D. Jud, A. Lauber, C. D. Bellicoso, V. Tsounis, J. Hwangbo, K. Bodie, P. Fankhauser, M. Bloesch, R. Diethelm, S. Bachmann, A. Melzer, and M. Hoepflinger, "Anymal - a highly mobile and dynamic quadrupedal robot," in *2016 IEEE/RSJ International Conference on Intelligent Robots and Systems (IROS)*, 2016, pp. 38–44.

[11] G. Bledt, P. M. Wensing, S. Ingersoll, and S. Kim, "Contact model fusion for event-based locomotion in unstructured terrains," in *2018 IEEE International Conference on Robotics and Automation (ICRA)*, 2018, pp. 4399–4406.

[12] M. Camurri, M. Fallon, S. Bazeille, A. Radulescu, V. Barasuol, D. G. Caldwell, and C. Semini, "Probabilistic contact estimation and impact detection for state estimation of quadruped robots," vol. 2, no. 2, 2017, pp. 1023–1030.

[13] M. Maravgakis, D.-E. Argiropoulos, S. Piperakis, and P. Trahanias, "Probabilistic contact state estimation for legged robots using inertial information," in *2023 IEEE International Conference on Robotics and Automation (ICRA)*, 2023, pp. 12 163–12 169.

[14] A. De Luca, A. Albu-Schaffer, S. Haddadin, and G. Hirzinger, "Collision detection and safe reaction with the dlr-iii lightweight manipulator arm," in *2006 IEEE/RSJ International Conference on Intelligent Robots and Systems*, 2006, pp. 1623–1630.

[15] S. Haddadin, A. De Luca, and A. Albu-Schäffer, "Robot collisions: A survey on detection, isolation, and identification," vol. 33, no. 6, 2017, pp. 1292–1312.

[16] S. Haddadin, A. Albu-Schaffer, A. De Luca, and G. Hirzinger, "Collision detection and reaction: A contribution to safe physical human-robot interaction," in *2008 IEEE/RSJ International Conference on Intelligent Robots and Systems*, 2008, pp. 3356–3363.

[17] J. Hwangbo, C. D. Bellicoso, P. Fankhauser, and M. Hutter, "Probabilistic foot contact estimation by fusing information from dynamics and differential/forward kinematics," in *2016 IEEE/RSJ International Conference on Intelligent Robots and Systems (IROS)*, 2016, pp. 3872–3878.

[18] F. Jenelten, J. Hwangbo, F. Tresoldi, C. D. Bellicoso, and M. Hutter, "Dynamic locomotion on slippery ground," *IEEE Robotics and Automation Letters*, vol. 4, no. 4, pp. 4170–4176, 2019.

[19] T. Lin, R. Zhang, J. Yu, and M. Ghaffari, "Deep multi-modal contact estimation for invariant observer design on quadruped robots," *CoRR*, vol. abs/2106.15713, 2021.

[20] L. Manuelli and R. Tedrake, "Localizing external contact using proprioceptive sensors: The contact particle filter," in *2016 IEEE/RSJ International Conference on Intelligent Robots and Systems (IROS)*, 2016, pp. 5062–5069.

[21] K.-L. Lu, I.-C. Chang, W.-S. Yu, and P.-C. Lin, "Trajectory optimization strategy that considers body tip-over stability, limb dynamics, and motion continuity in legged robots," in *2024 IEEE International Conference on Robotics and Automation (ICRA)*, 2024, pp. 5773–5779.

[22] Y.-S. Shen, W.-S. Yu, and P.-C. Lin, "Contact force estimation for a leg-wheel transformable robot with varying contact points," in *2025 IEEE International Conference on Robotics and Automation (ICRA)*, 2025, pp. 684–690.

[23] Y.-L. Lai, W.-S. Yu, and P.-C. Lin, "Stair climbing of a transformable robot using varying leg-wheel contact points," in *2025 IEEE International Conference on Robotics and Automation (ICRA)*, 2025, pp. 7675–7681.